Cement and Concrete Research 143 (2021) 106405

Contents lists available at ScienceDirect

Cement and Concrete Research

journal homepage: www.elsevier.com/locate/cemconres

Local structure and Ca/Si ratio in C-S-H gels from hydration of blends of tricalcium silicate and silica fume

Ana Cuesta [a,*], Isabel Santacruz [a], Angeles G. De la Torre [a], Monica Dapiaggi [b], Jesus D. Zea-Garcia [a], Miguel A.G. Aranda [a]

[a] Departamento de Química Inorgánica, Universidad de Málaga, Campus Teatinos S/N, 29071 Málaga, Spain
[b] Dipartimento di Scienze della Terra "Ardito Desio", Università degli Studi di Milano, Milano, Italy

ARTICLE INFO

Keywords:
Pair distribution function
Synchrotron radiation
Nanostructure
Amorphous material
Pozzolanic reaction
SCMs

ABSTRACT

At the microscale, C-S-H gels from alite, or neat Portland cements, has a Ca/Si ratio close to 1.80. At the nanoscale, C-S-H is described by a defective tobermorite structure which allows a maximum Ca/Si ratio close to 1.40. There is no agreement in the location of the extra 0.40 mol of $Ca(OH)_2$ at the nanoscale. Atomistic modelling studies reported $Ca(OH)_2$ species within the tobermorite interlayer space. Other works point toward a fine intermixing of defective tobermorite and nanoportlandite. Here, we have prepared a series of alite blended with silica fume and studied the pastes by several techniques including synchrotron pair distribution function (PDF). In the employed conditions, the C-S-H gel formed by the pozzolanic reaction has nearly the same local structure than the primary C-S-H gel. Furthermore, differential PDF points toward $Ca(OH)_2$ excess having a local structure compatible with few-layer thick nanoparticles stretched along the *c*-axis.

1. Introduction

Cement industry can be considered one of the major contributors for greenhouse gases emissions because for every ton of type-I grey Portland cement (PC), ~0.95 CO_2 tones are released into the atmosphere. This translates into ~7% of the total anthropogenic CO_2 emissions [1,2]. Consequently, CO_2 footprint reduction in the cement industry has been identified as a core need in the mitigation of the consequences of the coming climate crisis [1,3,4]. One possibility to reduce the embodied carbon content of mortars and concretes is the use of supplementary cementitious materials (SCMs) that can be used as partial clinker substitution [5–8] or can be added separately in the concrete mixer [9]. SCM materials have been identified by United Nations Environment Program Sustainable Building and Climate Initiative (UNEP-SBCI) [3] as the most favourable strategy for lowering CO_2 emissions in the cement industry with the lowest economic and performance impacts.

SCMs are reactive siliceous, aluminosiliceous, or calcium aluminosiliceous materials with hydraulic or pozzolanic properties. Research on these systems is becoming increasingly important [5–7]. A wide variety of materials are available to be used as SCMs [5], mainly silica fume, ground granulated blast furnace slag, fly ash, calcined natural minerals, biomass ashes and other industrial byproducts and wastes [7].

Tricalcium silicate, Ca_3SiO_5 or C_3S, is the main phase in PC [10]. The main hydration reactions of C_3S consists of its dissolution, the supersaturation of the medium with the ionic species and finally, the formation of the nanocrystalline/amorphous calcium-silicate-hydrate (C-S-H) gel, jointly with the crystallization of portlandite, $Ca(OH)_2$ according to Eq. (1). This C-S-H gel has been reported to be composed by defective nanocrystalline clinotobermorite, amorphous (monolayer) calcium hydroxide and gel pore water [11]:

$$\underset{Crystalline}{Ca_3SiO_5 + 5.2H_2O} \rightarrow \underset{}{1.2Ca(OH)_2} + \underset{C\text{-}S\text{-}H\ gel\text{–}nanocrystalline//amorphous}{1/9\left[Ca_{11}Si_9O_{28}(OH)_2 \cdot 8.5H_2O\right]//0.58\left[Ca(OH)_2\right]//2.37H_2O} \quad (1)$$

* Corresponding author.
E-mail address: a_cuesta@uma.es (A. Cuesta).

https://doi.org/10.1016/j.cemconres.2021.106405
Received 8 October 2020; Received in revised form 18 February 2021; Accepted 20 February 2021
Available online 6 March 2021

The two main products of reaction (1) are nanocrystalline C-S-H gel and crystalline portlandite. On the one hand, C-S-H gel from alite hydration at the microscale is known to have an average Ca/Si ratio of 1.70–1.80, a water content close to 4.0 mol per mol of SiO_2 and a density ranging 1.90–2.10 g cm^{-3}, depending upon the water-to-cement (w/c) mass ratio [10,12,13]. However, at the nanoscale, several investigations concluded that C-S-H is better described by a defective tobermorite structure. It is reminded that the Ca/Si ratio in crystalline tobermorites ranges between 0.67 and 0.83 [14–16]. Defect-containing tobermorite and clinotobermorite can increase this ratio to values close to 1.4 [17]. There is no agreement in the location of the extra 0.40 mol of $Ca(OH)_2$ at the nanoscale. On the one hand, there are reports suggesting Ca-containing species within the tobermorite interlayer space from atomistic studies. An initial molecular dynamics study for C-S-H [18] was followed by molecular dynamics and density functional theory works for C-S-H [19] and C-A-S-H [20] where the individual building blocks were identified allowing the calculation of theoretical NMR spectra for comparison with experiment NMR data. On the other hand, there are studies pointing toward a fine intermixing of defective tobermorite particles with nanoportlandite (single layer or just a few layers) [11,21–23]. The difference between these approaches to describe C-S-H at the nanoscale is the location of the $Ca(OH)_2$ species within the defective tobermorite particles or outside.

Additionally, crystalline portlandite is known to have defects in the packing along the *c*-axis which results in anisotropic peak broadening of its X-ray powder diffraction pattern [24]. Furthermore, and very interestingly, it has been very recently reported that under very high supersaturation conditions amorphous $Ca(OH)_2$ and/or a metastable nanocrystalline $Ca(OH)_2$ precede the formation of stable crystalline portlandite [25]. This process takes place through a nonclassical aggregation mechanism, called as "oriented attachment". However, the occurrence of this nucleation pathway in real cement hydrating conditions remains to be established.

The calcium hydroxide formed in reaction (1) can be (partly) employed to generate additional secondary C-(A)-S-H through the pozzolanic reaction with SCMs. The kinetics of this reaction depends on several factors such as the chemical composition of SCM(s), the fineness and the amount of the involved phase, and hydrating temperature, among others [7]. Specifically, silica fume (SF) consists nearly exclusively of amorphous SiO_2 of very fine particle size, sub-micrometre, and it has been demonstrated to present a high pozzolanic activity. This reaction leads to the formation of a secondary C-S-H, although the stoichiometry of the gel is not well known and its composition is not easy to determine [26,27] in the presence of large amount of primary C-S-H. Previously, it was reported [8] that the simplest pozzolanic reaction using a siliceous material, such as silica fume, progresses according to reaction (2):

$$SiO_2 + 1.7\ Ca(OH)_2 + 2.3\ H_2O \rightarrow (CaO)_{1.7}SiO_2 4H_2O \quad (2)$$

However, it has been reported that the presence of SCM leads to a decrease of the Ca/Si ratio of the C–S–H gel [28–30] with important changes in the microstructures as revealed by transmission electron microscopy. For PCs/SF blends, the Ca/Si ratio of this secondary C-S-H gel was found to be ≈1.40–1.50 as crystalline portlandite is consumed by SF [29]. Ca/Si ratio of this gel can drop down as low as ≈1.00 in absence of any $Ca(OH)_2$ [29]. These results clearly indicate that the excess of $Ca(OH)_2$, independent of its local structure, is highly reactive toward the pozzolanic reaction.

During the first hours of hydration, the presence of SF particles provides an extra surface, known as seeding effect [31,32], that accelerates the hydration reaction of tricalcium silicate by providing heterogeneous nucleation sites for the main hydration product, C–S–H gel, to form and grow [26,30,33]. The formation of the secondary C-S-H gel due to the pozzolanic reaction occurs at later ages due to the slower dissolution of SF. In Portland cement-silica fume blend systems, the reduction of portlandite due to pozzolanic reaction has been observed since 1 day of hydration [34]. Moreover, these authors observed that the amount of silica fume that participated in the pozzolanic reaction was close to 4%–5% and the excess added was used to fill the pores in the system. The addition of SF in cements can improve the mechanical strength of mortars and concretes but only when the optimal amount of this SCM is added [34,35]. The degree of reaction of SF can be followed by ^{29}Si MAS NMR since the broad resonance from silica fume, located from −100 to −125 ppm, does not overlap with the peak signals of anhydrous phases or C–S–H gel [26,30] located between −90 and − 68 ppm.

Finally, synchrotron pair distribution function (SPDF) methodology [36,37] is a tool that has been recently used for understanding the binder local structures of the cement gels by synchrotron radiation approaches [11,38]. SPDF has been employed to characterize the local structure of C–S–H gels [11,23,39–41] in different tricalcium silicate samples. The main conclusion of these works was that the C–S–H gel has a nanocrystalline nature with an atomic local ordering close to 4 nm [39,42]. Moreover, the C-S-H gel obtained from the hydration of C_3S was reported to contain mainly two components: a nanocrystalline defective clinotobermorite, $Ca_{11}Si_9O_{28}(OH)_2{\cdot}8.5H_2O$, and an amorphous component with an atomic local order close to monolayers of calcium hydroxide [11,23]. SPDF methodology has also been used in blended C_3S–slag and alkali activated slag in order to establish the nature of C-A-S-H and C-(N)-A-S-H gels. In this work, C-A-S-H showed a long range ordering being nanocrystalline (as C–S–H) in comparison to the C-(N)-A-S-H gel which was found to be mainly amorphous [43].

The main aim of this work is to determine the changes in the local order of the C–S–H gels formed from the hydration of blends of tricalcium silicate with silica fume by varying the overall Ca/Si ratio. The pozzolanic reaction of crystalline (and amorphous) portlandite with silica fume to form secondary C-S-H gel is investigated at four months of hydration, i.e. after full reaction of the silica fume. ^{29}Si MAS-NMR, thermal analysis and transmission electron microscopy techniques are used to characterize the resulting pastes. SPDF methodology is essential in this work to unveil the changes in the local structure of the resulting gels.

2. Experimental section

2.1. Sample description and preparation

$Ca(OH)_2$, ACS reagent with a purity ≥ 95.0%, was purchased from Honeywell Fluka to be used as reference. Triclinic tricalcium silicate, t-C_3S, was purchased from Mineral Research Processing (M.R.PRO). Two different silica fume (SF) powder samples were used in this study: i) densified silica fume supplied by FerroAtlántica S.A.U. (hereafter named SF_F), now called as Xallas Electricidad y Aleaciones S.A.U. (Xeal), with a 90.1 wt% purity in SiO_2, determined by XRF, see Table S1, and ii) undensified silica fume 940U supplied by Elkem Iberia (hereafter named SF_E) with a 96.8 wt% purity in SiO_2, see Table S1.

Beta (monoclinic) dicalcium silicate, β-C_2S, was synthesized using SiO_2 (Alfa Aesar, 99.5%), $CaCO_3$ (Alfa Aesar, 99.95–100.05%) and γ-Al_2O_3 (Alfa Aesar, 99.999%) as raw materials in the stoichiometric proportions to give $Ca_2Si_{0.972}Al_{0.028}O_{3.986}\square_{0.014}$ as previously reported [44] where the symbol □ stands for vacancies. Around 215 g of raw materials were mixed in a Micro-deval mill (Model A0655, Proeti) using a 1 L jar (without balls) for 30 min and the powders were preheated for 4 h up to 1050 °C with a heating rate of 10 °C/min. Then, the material was ground for 45 min using the Micro-deval device using the 1 L jar with stainless steel balls (12 units of 18 mm and 5 units of 30 mm) to obtain a better homogenization. The sample was heated up to 1500 °C for 6 h after pressing the powder into 6 cm diameter pellets with an average thickness of ~1 cm. The material was quenched from high temperature with an air flow. The resulting pellets were ground in batches of 50 g in a disk mill (Model T8.100, Siebtchnik). Again, new pellets were prepared, heated up to 1200 °C for 1 h with a heating rate of

20 °C/min, quenched with an air flow and ground in the disk mill. Finally, an additional cycle was carried out and new pellets were prepared, heated up to 1000 °C for 30 min and cooled with liquid nitrogen. These pellets were ground again in the disk mill.

2.1.1. Preparation of concentrated silica fume suspensions

Concentrated SF_F and SF_E suspensions (24.22 wt%: 66 g H_2O and 21.09 g SF) were prepared as follows. SF powder was slowly added into double-boiled water while stirring in a mechanical stirrer. It was kept stirring (800 rpm) for 5 min. After that, a professional hand-blender (Dynamix DMX 160 v2, with a two-wing blade) was used at 13,000 rpm. The plastic beaker with the suspension was introduced in a cold water bath (with ice) to avoid heating during blender application. The hand-blender was used for a total of 16 min for SF_F, and 12 min for SF_E. In both cases, the blending was carried out in steps of 2 min with 1 min of resting time to avoid overheating and thus extra agglomeration. Finally, 1 min of ultrasound (UIP1000hd ultrasound probe, Hielscher) with 50% amplitude was applied to both SF suspensions, applied in steps of 10 s, and the plastic beakers were introduced in an ice water bath during ultrasonication.

2.1.2. Preparation of pastes of C_3S/SF blends

t-C_3S/SF pastes were prepared with varying overall Ca/Si ratios (see Table 1). In order to do that, four aliquots of the same concentrated SF suspensions, prepared as described above, were taken and diluted (Table 1) with double-boiled water. The concentrated SF suspensions were mechanically stirred at 400 rpm before the aliquots were taken. During the preparation of the different pastes, both concentrated suspensions were kept in a shaker. Firstly, t-C_3S powder was added to the diluted SF suspensions (Table 1) and then, the paste was mechanically stirred for 90 s at 1600 rpm, with 30 s pause, followed by another 90 s stirring at 1600 rpm. Secondly, the resulting pastes were introduced into hermetically closed cylindrical molds which were rotated at 16 rpm for 5 days. Finally, cylinders were taken out and stored within demineralized (and double-boiled) water. Pieces were taken out at four months of hydration. The amounts of every component are summarized in Table 1. The numbers in the labels of each sample stand for the Ca/Si nominal ratio.

In addition, two reference pastes were prepared without SF. t-C_3S paste was prepared using 10.00 g of C_3S and 8.20 g of double-boiled water. The paste was removed from the mold after 7 days. Then, the cylinders were covered with paraffin and introduced in double-boiled water for another 15 days. At this stage, the paraffin was removed and cylinders were introduced in double-boiled water up to 4 months.

After four months of hydration, the cylinders were taken out of the water and dried with laboratory paper. Then, the pastes were gently ground in an agatha mortar and immediately loaded in the capillaries for the PDF study. It is highlighted that the hydration reactions were not further arrested by any other methodology like freeze drying or solvent exchange to avoid altering/damaging C-S-H.

β-C_2S paste was prepared as previously explained for the t-C_3S using a water-to-solid (w/s) mass ratio of 0.45, see Table 1. The cylinder was ground at 12 months of hydration and immediately introduced in the capillaries without a further hydration arresting stage.

2.2. Synchrotron X-ray powder diffraction (SXRPD)

SXRPD patterns were collected in Debye-Scherrer (transmission) mode using the X-ray powder diffraction endstation of BL04-MSPD beamline at ALBA synchrotron (Barcelona, Spain) [45]. The wavelength, 0.41318(1) Å, was selected with a double-crystal Si (111) monochromator and determined by using Si640d NIST standard (a = 5.43123 Å). The diffractometer is equipped with a MYTHEN detector especially suited for time-resolved and good signal-to-noise ratio experiments. The borosilicate glass capillaries, 0.7 mm of diameter, were rotated during data collection to improve diffracting particle statistics. For the Rietveld quantitative phase analysis studies of C_3S-SF pastes, three SXRPD patterns were collect at three different positions of every capillary and merged to produce the final dataset. No changes were observed among the individual patterns. The total acquisition time was 6 min per dataset (2 min per pattern) over the angular range 1–30° (2θ). For the Rietveld studies, samples were previously mixed with ~20 wt% of α-Al_2O_3 (AlfaAesar) as internal standard. The standard, α-Al_2O_3, was previously heated up to 1500 °C for 20 h and sieved <125 μm.

For the PDF study, SXRPD data were collected for ~3 h per sample. Five patterns were collected for each sample (four in the case of C_2S-0SF-2.0 paste and three for the anhydrous samples), each lasted ~40 min, and merged in order to improve the signal-to-noise ratio in the recorded very wide angular range, 1 to 130° (2θ). No changes among individual patterns were observed.

Laboratory X-ray powder diffraction (LXRPD) data for C_2S-0SF-2.0 paste mixed with ~15 wt% of quartz as internal standard was collected on a D8 ADVANCE (Bruker AXS) diffractometer (SCAI – Universidad de Malaga) equipped with a Johansson monochromator, using strictly monochromatic MoKα$_1$ radiation, λ = 0.7093 Å, in transmission geometry (θ/θ).

2.3. Rietveld data analysis

Rietveld quantitative phase analyses (RQPA) were performed using the GSAS suite of programs and the EXPGUI graphic interface [46]. Background coefficients, zero-shift error, cell parameters and peak shape parameters (using a pseudo-Voigt function) were refined [47]. The non-crystalline content (amorphous and nanocrystalline, ACn) was determined by the internal standard methodology [48].

Table 1
Dosages for the preparations of the pastes studied in this work.

Sample[a]	Concentrated SF suspension (g)	Added water[b] (g)	C_3S or C_2S (g)	Total H_2O (g)	SF (g)	Total H_2O + SF (g)	w/C_3S or w/C_2S ratio[d]	w/s[c]	Ca/Si nominal ratio
C_3S-0SF-3.0	–	–	10.00	8.20	–	8.20	0.82	0.82	3.00
C_3S-SF_E-2.4	3.02	6.71	10.00	9.00	0.73	9.73	0.90	0.84	2.36
C_2S-0SF-2.0	–	–	10.00	4.50	–	4.50	0.45	0.45	2.00
C_3S-SF_E-1.8	8.12	4.44	10.00	10.60	1.96	12.56	1.06	0.89	1.75
C_3S-SF_E-1.5	12.10	2.82	10.00	12.00	2.92	14.92	1.20	0.93	1.45
C_3S-SF_F-1.5									1.50
C_3S-SF_E-1.2	17.40	–	10.00	13.20	4.20	17.40	1.32	0.93	1.19
C_3S-SF_F-1.2									1.22

[a] **SF_E** and **SF_F** stand for **S**ilica **F**ume from **E**lkem and from **F**erroAtlantica suppliers, respectively.
[b] Additional water added to dilute the concentrated suspension.
[c] s stands for the overall solid content, i.e. C_3S + SF or C_2S + SF.
[d] w/C_3S stands for the overall water-to-C_3S mass ratio.

2.4. Pair distribution function data analysis

PDF experimental data were obtained using PDFgetX3 [49] with $Q_{max} = 21$ Å^{-1}. The subtraction of PDF patterns were done with D1Dplot software [50]. Simulations of nano-portlandite were obtained using Diffpy-CMI [51] for discrete particles of single-layer and two-layer portlandite, with no periodicity. The nanoparticles had variable dimensions along the [100], [010] and [001]. Thermal displacement parameters have a very important influence on the amplitude of the atom-atom correlations. For this reason, they have been fixed to reasonable small values. In particular, the selected U values were 0.009 Å^2 and 0.011 Å^2, for Ca and O atoms, respectively. Moreover, thermal displacement parameters values were varied, in the range ± 0.2 Å^2 (B_{iso} values), and no significant differences were found on the resulting PDFs.

2.5. Thermal analysis (TA)

Differential thermal analysis (DTA) and thermogravimetric analysis (TGA) measurements for the pastes (without arresting the hydration) were performed in a SDT-Q600 analyzer from TA instruments (New Castle, DE). The temperature was varied from RT to 1000 °C at a heating rate of 10 °C/min. Measurements were made in open platinum crucibles under synthetic air flow.

2.6. Particle size distribution (PSD) analysis

The particle size distribution of the samples was measured by laser diffraction (Malvern MasterSizer S, UK) provided with a wet chamber. Powders were previously dispersed in isopropanol using an ultrasonic bath.

2.7. BET surface area determination

The specific surface area of the samples was measured by multi-point N_2 adsorption with a BET (ASAP 2420, Micromeritics, USA) instrument.

2.8. X-ray fluorescence (XRF) analysis

The elemental composition of the samples was measured by XRF using an ARL ADVANT'XP+ (Thermo Fisher) equipment at the SCAI – Universidad de Málaga.

2.9. Electron microscopy study

High resolution transmission electron microscopy (HR-TEM) measurements were carried out using a FEI Talos F200X microscope, operating at 200 kV, equipped with X-FEG electron source and super-X EDS (Energy Dispersive Spectroscopy) system with four silicon drift detectors (SDDs) for microanalysis.

2.10. MAS-NMR study

^{29}Si MAS-NMR (Magic Angle Spinning Nuclear Magnetic Resonance) spectrum for all the samples was recorded at RT on a Bruker AVIII HD 600 NMR spectrometer (field strength of 14.1 T) at 156.4 MHz. The chemical shift was referenced to an external solution of tetramethylsilane.

3. Results

3.1. Starting and reference sample characterization

Anhydrous products were initially characterized by laboratory techniques. Triclinic tricalcium silicate material had a BET specific surface area (SSA) of 1.9(1) m^2 g^{-1} and a $d_{v,50}$ of 4.6 μm whose PSD is shown in Fig. S1a (Supplementary information). Fig. S2 displays the Rietveld fit of the LXRPD data for t-C_3S showing that it is a single crystalline phase. Moreover, the PDF signal for this sample in the r-range between 1 and 10 Å is showed in Fig. S3. SF_E has a BET specific surface area of 23.4(1) m^2 g^{-1} and an average density of 2.29(1) g cm^{-3}. Its PSD is displayed in Fig. S1b having a $d_{v,50}$ of 1.3 μm. The LXRPD data showed that this material is mainly amorphous as only small diffraction signals can be observed which correspond to Si and SiC, see Fig. S4. SF_F has a BET specific surface area of 27.4(2) m^2 g^{-1} and an average density of 2.36(1) g cm^{-3}. The measured $d_{v,50}$ is 4.1 μm and the PSD analysis is shown in Fig. S1c. The LXRPD data for this phase is showed in Fig. S4. As some crystalline reflections were found for this material, a LXRPD analysis jointly with the internal standard methodology was also performed for SF_F, see Fig. S5. The Rietveld quantitative phase analysis is shown in Table S2. Both PDF signals for SF samples are displayed in Fig. S3. For beta dicalcium silicate, the obtained $d_{v,50}$ was 2.4 μm, see Fig. S1d, and the BET area was 2.3(1) m^2 g^{-1}. Fig. S6 displays the Rietveld fit for this sample that showed that the sample had a purity of 99.3(1) wt% with an additional 0.7(2) wt% of gamma dicalcium silicate.

The characterization of commercial portlandite was also carried out. The $d_{v,50}$ was 2.7 μm, see Fig. S7, and the BET area was 17.0(1) m^2 g^{-1}. Fig. S8 displays the DTA-TGA data of this sample. The region between 550 °C and 1000 °C shows a weight loss of 0.93% which correspond to 2.1 wt% of $CaCO_3$. The XRF data for this sample are reported in Table S1 and the Rietveld fit is shown in Fig. S9. A structural refinement was performed for this sample. Atomic displacement parameters and atomic positions were also refined. Moreover, Fig. S10 shows the PDF signal for this commercial portlandite jointly with simulated references for the sake of comparison. Some significant differences are highlighted in the figure.

The SSA and PSD measurements indicate that SF_E, SF_F and portlandite are heavily agglomerated. The average diameter, D_{BET}, can be calculated (assuming monodisperse spherical primary particles) according to the equation reported in [52], $D_{BET} = 6 / SSA \cdot \rho$. The obtained D_{BET} values for SF_E, SF_F and portlandite are 112, 93 and 158 nm, respectively.

The experimental synchrotron PDF pattern of crystalline calcium hydroxide presents the Ca···Ca interatomic distance peak at 6.16 Å, see Table 2, which is much higher than that calculated after Rietveld refinement, which is 6.11 Å and that found for the structure reported in the CIF with ICSD collection code #202220 [53] whose crystal structure was obtained by single crystal neutron diffraction. This difference is mainly due to the defects in crystal packing along the *c*-axis which were known [24,53] and yielded anisotropic peaks in the synchrotron powder patterns.

3.2. Hydrated pastes characterization

3.2.1. ^{29}Si MAS-NMR

All the hydrated pastes including the anhydrous materials, were

Table 2
Ca···Ca interatomic distances obtained from the different PDF plots.

PDF pattern		Ca···Ca *c*-axis interatomic distance (Å)
$Ca(OH)_2$	From CIF #202220, neutron single crystal, averaged	6.10
$Ca(OH)_2$ sample	From Rietveld data this study, averaged – commercial	6.11
$Ca(OH)_2$	From PDF, local – commercial sample	6.16
C_3S-0SF-3.0	From differential[a] PDF, local – paste	6.18
C_3S-SF_E-2.4	From differential[a] PDF, local – paste	6.19
C_2S-0SF-2.0	From differential[a] PDF, local – paste	6.24
C_3S-SF_E-1.8	From differential[a] PDF, local – paste	6.18

[a] Differential PDFs are calculated using the raw PDF pattern of C_3S-SF_E-1.2 sample to subtract the C-S-H signal of the other pastes. See Section 3.2.5 for more details.

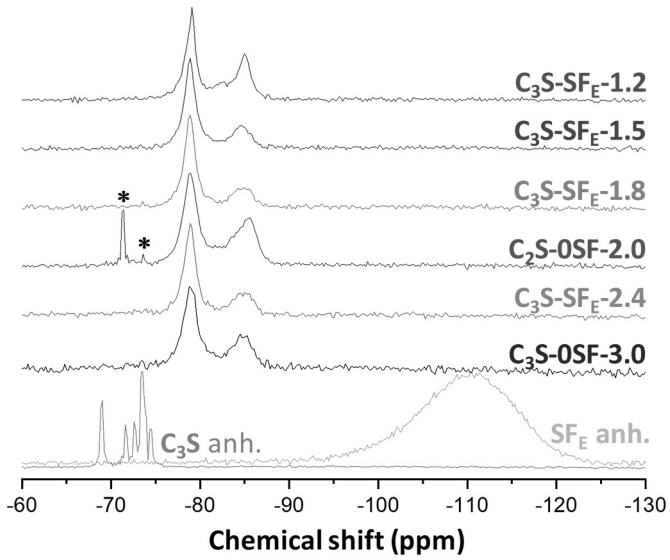

Fig. 1. ^{29}Si MAS-NMR spectra for C_3S-SF_E pastes including anhydrous materials. The asterisks highlight the presence of unreacted belite. Spinning rate of 15 kHz and a magnetic field of 14.1 T. The spectra have been vertically displaced for clarity.

initially studied by ^{29}Si MAS-NMR. Fig. 1 shows the ^{29}Si MAS-NMR spectra obtained for the series of SF_E hydrated pastes (including anhydrous t-C_3S and SF_E). The signal situated at ~−110 ppm, which correspond to SF [26], is negligible in all the hydrated pastes which proves that this phase has fully reacted at 4 months of hydration. The same behaviour was observed for the hydrated pastes with the addition of SF_F, see Fig. S11. It can also be stated that C_3S has a hydration degree larger than 95% for all samples after 4 months, but this is not the case of belite where a small fraction of anhydrous component remains even after 12 months of hydration at room temperature.

The signals observed at approximately −79 and − 85 ppm are attributed to the Q^1 and Q^2 Si units, respectively [54,55]. Q^1 is associated with silicate end chain units and Q^2 indicates the presence of silicate in intermediate chain positions [56,57]. The silicate mean chain length (MCL) can be determined from the expression, $MCL = 2(Q^1 + Q^2) / Q^1$ or $MCL = 2(Q^1 + Q^2 + (3/2)Q^2(1Al)) / Q^1$ [56]. The deconvolution of the spectra shown in Fig. 1 gives the areas for these bands reported in Table 3 which allow to determine the MCLs. The individual fits, for every hydrated sample spectrum, are displayed in Fig. S12a–f.

3.2.2. DTA-TGA

The thermogravimetric data for all the hydrated pastes are shown in Fig. 2. Moreover, Figs. S13–S20 show the full DTA-TGA data including the derivative of weight and heat flow signals for all the pastes. Table 4 shows the overall measured weight losses as well as the break down in the different temperature ranges. Firstly, the weight loss from RT to 250 °C was considered to correspond to free water and C-S-H gel. The range between 400 and 550 °C was used to calculate the weight loss of crystalline portlandite with the tangential method. This methodology is considered the best method to quantify this phase by thermal approach [58]. This weight loss value is obtained from the difference of the tangential lines (top and bottom) at the position of the centre of the main peak in the derivative weight loss curve, see Figs. S13–S20. The calculated amount of portlandite by thermal analysis is given in Table 5. Finally, the very small losses between 550 °C and 1000 °C likely corresponds to a final dehydroxylation of C-S-H gel and decomposition of any (very minor) amount of calcium carbonate from partial carbonation of $Ca(OH)_2$. It is noteworthy by simple observation that the sample C_3S-SF_E-1.8 has much larger portlandite content than hydrated belite. This observation has important implications for the Ca/Si ratios in C-S-H gels that will be discussed below. We speculate that this could be related to the different hydration rates but further research is needed to establish the origin of this puzzling result. Finally, it is also important to notice that hydrated belite has a much larger weight loss between 250 and 400 °C that any other paste, see Figs. 2, S20 and Table 4.

Table 3
Summary of the ^{29}Si MAS-NMR results for the studied samples.

Sample	Q^1 position/ppm	Q^1 area/%	Q^2 (1Al)/Q^2 position/ppm	Q^2 (1Al)/Q^2 area/%	MCL
C_3S-0SF-3.0	−79.2	68.2	–/−85.1	–/31.8	2.93
C_3S-SF_E-2.4	−78.9	72.7	–/−84.9	–/27.3	2.75
C_2S-0SF-2.0[a]	−78.9	52.9	−84.0/−85.6	19.1/19.0	3.80
C_3S-SF_E-1.8	−78.8	76.1	–/−84.8	–/23.9	2.63
C_3S-SF_E-1.5	−78.8	71.6	–/−84.6	–/28.4	2.79
C_3S-SF_E-1.2	−79.0	54.9	−82.5/−85.0	10.8/34.4	3.84

[a] This spectrum also shows Q_0 bands (unreacted belite) located at −71.3 ppm (8.0%) and − 73.7 (1.0%).

3.2.3. Rietveld analysis of diffraction data

As described in the materials and method section, the hydrated pastes were mixed with ~20 wt% of Al_2O_3 as internal standard in order to obtain the Rietveld Quantitative Phase Analysis (RQPA) including the ACn fraction. In the case of the β-C_2S paste, C_2S-0SF-2.0, this sample was mixed with ~15 wt% of quartz as internal standard. It has to be noted that the RQPA of the samples with internal standard yielded a value of total amorphous and nanocrystalline material which in this case includes, all the amorphous/nanocrystalline hydrated material but also the water that is not chemically bound, the free water (FW). Table S3 shows the RQPA results of all the samples. The FW values have been theoretically calculated according to the reacted amount of t-C_3S by using Eq. (1) which states that 5.2 mol of water is consumed by a mol of silicate and Eq. (3) which also includes the water needed for the pozzolanic reaction according to the silica fume consumed. The total amount of water used for the FW calculation is that reported in Table 4 as experimental total weight loss, see more details in the S.I. Figs. S21–S24 display the Rietveld plots for the final fits. The quantitative results for crystalline portlandite determined by Rietveld analysis are also given in Table 5. The consumption of portlandite and the increase of the ACn content along the series, prove again that the pozzolanic reaction (2) is taking place and it can be quantified. Alite hydration degree was 97% for C_3S-0SF-3.0 and steadily increases to 99% for C_3S-SF_E-1.2.

Table 5 also reports the expected bulk Ca/Si ratio in the resulting C–S–H gel at the micrometre scale, taken into account the overall stoichiometry and the remaining fraction of crystalline (micrometre sized) portlandite, obtained from the average values of Rietveld and DTA analyses, assuming the following reaction:

$$C_3S + [(1+y)*4 + (3 - ((1+y)*z))]H + yS \rightarrow [3 - ((1+y)*z)]CH + (1+y)C_zSH_4 \quad (3)$$

where y is already known because it is the initial amount of added SF and has totally reacted, for each paste, and z can be estimated by comparison of theoretical values of crystalline portlandite with the average fractions determined by DTA and RQPA. The estimated z values are those whose amounts of crystalline portlandite compared best with the experimental values obtained in this study. Calculations for C_3S-0SF-3.0 and C_3S-SF_E-2.4 samples are detailed in the S.I. as examples.

It is worth to highlight that the w/c mass ratios employed for the preparations of these pastes were calculated according to reactions (1) and (2), using the $C_{1.8}SH_4$ stoichiometry, and then, these amounts were doubled, see Table 1. This choice was done because a relatively large w/s ratio will lead to full reaction in the studied hydration times. Belite sample was hydrated using a w/s mass ratio of 0.45 which is quite close to the stoichiometric amount of water needed for full reaction.

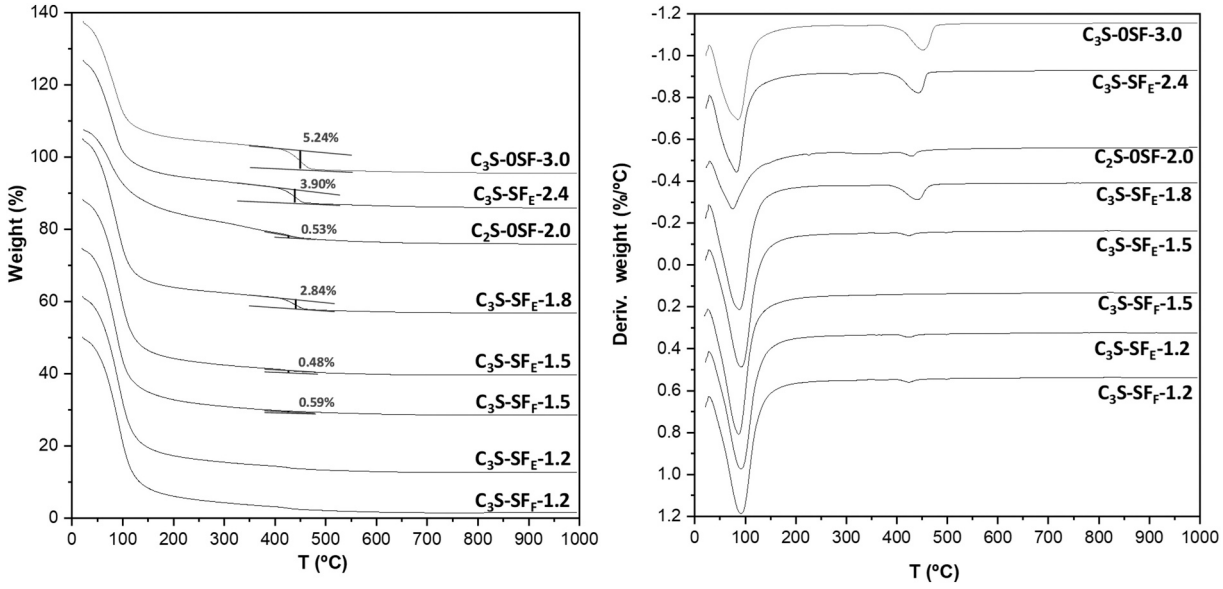

Fig. 2. Thermogravimetric traces for the series SF-C_3S hydrated pastes and belite paste. (Left) The black traces are the weight losses with temperature and blue lines represent the weight losses of the crystalline portlandite, determined by the tangential method. The traces have been vertically displaced for clarity. (Right) Derivatives of the weight losses for the studied samples. (For interpretation of the references to color in this figure legend, the reader is referred to the web version of this article.)

Table 4
Experimental weight losses (%) in the selected ranges obtained by TGA for all pastes.

Sample	Nominal water added[a]	Experimental total weight loss	Weight loss up to 250 °C	Weight loss 250–400 °C	Weight loss 400–550 °C	Weight loss 550–1000 °C
C_3S-0SF-3.0	45.1	42.1	33.1	2.0	**5.2**[b] + 1.1[c]	0.7
C_3S-SF_E-2.4	45.6	41.0	33.0	2.3	**3.9**[b] + 0.8[c]	0.9
C_2S-0SF-2.0	31.0	31.9	24.6	4.0	**0.5**[b] + 1.9[c]	0.9
C_3S-SF_E-1.8	47.0	48.4	42.2	1.9	**2.8**[b] + 1.0	0.6
C_3S-SF_E-1.5	48.2	48.7	45.2	1.9	**0.5**[b] + 0.8[c]	0.3
C_3S-SF_F-1.5	*48.2*	*45.4*	*41.3*	1.9	**0.6**[b] + 1.0[c]	*0.7*
C_3S-SF_E-1.2	48.2	46.2	43.0	1.8	0[b] − 0.8[c]	0.5
C_3S-SF_F-1.2	*48.2*	*45.3*	*42.1*	1.8	0[b] − 0.9[c]	*0.5*

[a] Calculated from the water to solid ratio in the initial mix, see S.I.
[b] Determined weight loss from the tangential method in the 400–550 °C temperature interval [58].
[c] Extra measured weight loss by TA analysis software in the 400–550 °C temperature interval.

Table 5
Weight percentage of crystalline portlandite determined from thermal analysis (tangential method) and Rietveld analysis. Resulting Ca/Si ratio within bulk C-S-H gel and comparison from transmission electron microscopy.

Sample	%CH – DTA-TGA	%CH – RQPA	%CH – average	Ca/Si ratio C-S-H gel Calculated	Ca/Si ratio C-S-H gel HR-TEM[a]	Ca/Si ratio Max–min HR-TEM	No. points HR-TEM
C_3S-0SF-3.0	21.6	24.8	23.2	1.70	1.78 (21)	2.26–1.45	38
C_3S-SF_E-2.4	16.0	14.4	15.2	1.66			
C_2S-0SF-2.0	2.2	2.5	2.4	1.90	1.82 (25)	2.49–1.50	66
C_3S-SF_E-1.8	11.7	11.6	11.6	1.25			
C_3S-SF_E-1.5	2.0	1.3	1.6	1.38	1.48 (35)	2.30–1.13	94
C_3S-SF_F-1.5	2.4	2.3	2.3	1.41			
C_3S-SF_E-1.2	0	0	0	1.20	1.06 (8)	1.27–0.88	45
C_3S-SF_F-1.2	0	0	0	1.20			

[a] The figures given within the brackets are the standard deviations calculated from all the measurements in a given specimen.

3.2.4. HR-TEM

Selected pastes were studied by high-resolution transmission electron microscopy with microanalysis capabilities. The results are also given in Table 5, where the average Si/Ca ratios of the C-S-H probed volumes are stated. It is important to notice the large spread in values, which is also reported in the table, which shows the intrinsic heterogeneity to these materials. Furthermore, the number of selected points (within the reported ranges) is also given. It can be seen that the average ratios match fairly well the calculate Ca/Si composition from the chemical reaction taken into account the portlandite consumption.

3.2.5. SPDF analysis of hydrated pastes

The low angle regions of the total scattering SXRPD, which span up to 130° (2θ), are given in Fig. 3. As expected, the decrease of crystalline portlandite content along the series is evident following the 4.8° and 9.0° (2θ) main reflections. The C_3S-SF_E-1.2 sample shows the absence of crystalline portlandite due to the complete reaction of this phase with the added silica fume. Consequently, this sample is mainly composed of C-S-H gel, according to chemical reactions (1) and (2), and it could be used as a reference for the C-S-H gel. Furthermore, the portlandite content variation correlates very well with the TGA and RQPA results reported just above. Notice the larger content of crystalline $Ca(OH)_2$ in C_3S-SF_E-1.8 than in hydrated belite, C_2S-0SF-2.0, as reported in Table 5 are directly evident in Fig. 2.

The key short interatomic correlations region of the raw synchrotron PDF data for the hydrated pastes is displayed in Fig. 4. This figure also includes the PDF pattern for commercial portlandite as reference. Data presented in Fig. 4 are derived from those shown in Fig. 3 and hence, the same evolution for crystalline portlandite is evidenced. It must be emphasized that the evolution along the series is the decrease of crystalline CH content and the increase of C-S-H content, both due to the pozzolanic reaction, see chemical reaction (2). Chiefly, the smooth variation in the traces, without the appearance of new interatomic correlations, allows us to conclude that the local structure for the C-S-H formed by the pozzolanic reaction is quite similar to that produced by the direct hydration of alite. Moreover, the lack of new interatomic distances correlations for C_3S-SF_E-1.2, see Fig. 4, and the simple shape of its scattering pattern, see Fig. 3, suggest that this could be a good approximation to the local structure of C-S-H gel. Finally and as expected, the Si—O interatomic correlation bands, located at 1.65 Å, increases in area, as the Ca/Si ratio decreases along the series, due to the larger C-S-H gel content.

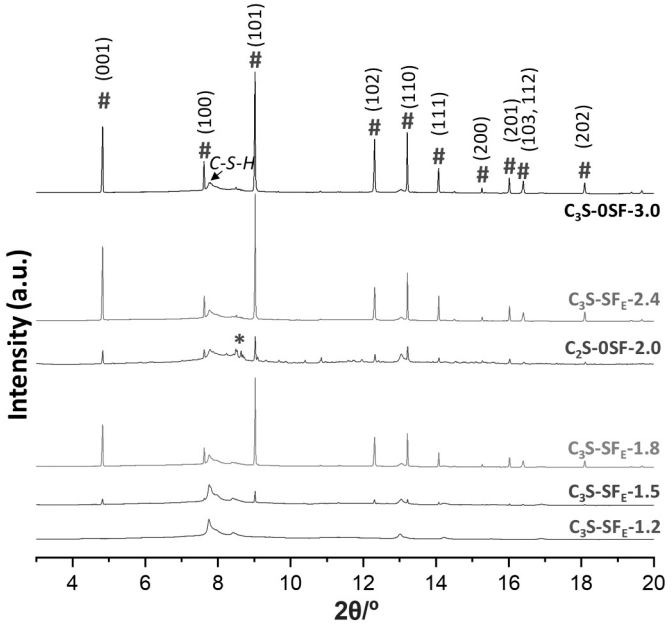

Fig. 3. Selected (low angle) region of the total scattering synchrotron powder diffraction patterns (λ = 0.41 Å) for the C_3S-SF_E hydrated pastes and C_2S_0SF_2.0 sample. The diffraction peaks of portlandite, $Ca(OH)_2$, and unreacted belite, Ca_2SiO_4, are highlighted with the symbols # and *, respectively. Patterns have been vertically displaced for clarity.

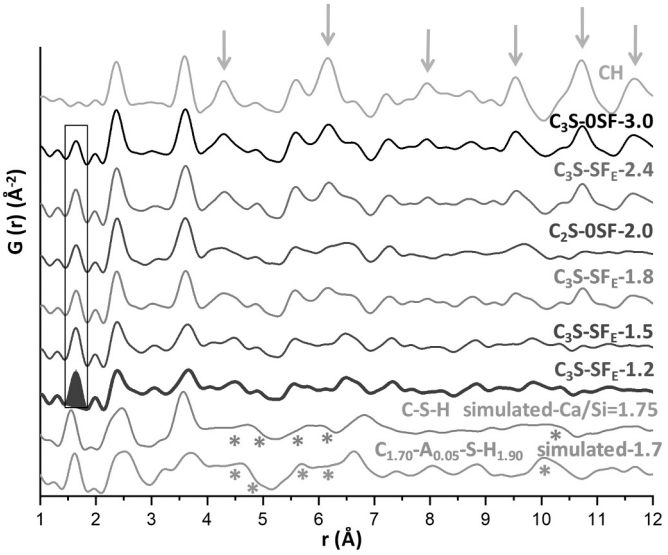

Fig. 4. Experimental synchrotron PDF patterns for the C_3S-SF_E pastes and C_2S_0SF_2.0 sample from 1 to 12 Å. The experimental plot for crystalline commercial portlandite is given at the top as reference. The theoretical PDF patterns for C-S-H and C-(A)-S-H are given at the bottom and they are calculated from the CIFs reported in [19,20], respectively. The main not overlapped interatomic correlations in portlandite are highlighted with arrows. The asterisks stand for main differences among simulated and experimental C-S-H patterns. The Si—O interatomic correlations, centred at 1.65 Å, are boxed.

The larger interatomic correlation distance, 12–30 Å, PDF region for the series is given in Fig. S25. As expected, samples with low amounts of crystalline portlandite show much lower overall crystallinity. The PDF patterns for the samples containing SF_F are displayed in Fig. S26. Although SF_E and SF_F samples have a different origin and the chemical

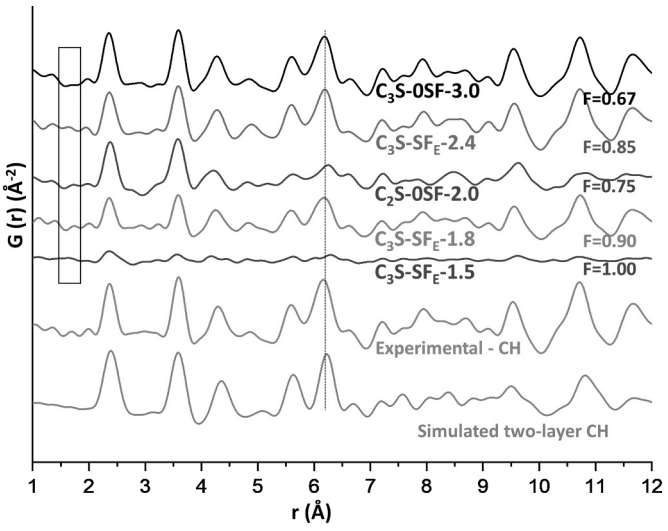

Fig. 5. Differential (subtracted) synchrotron PDF patterns using C_3S-SF_E-1.2 as reference to subtract. For details about the C-S-H contribution removal procedure, see the text. The PDF patterns for crystalline portlandite (experimental) and two-layer nanoportlandite (calculated) are given at the bottom. The black box highlights the absence of Si—O interatomic correlations due to the subtraction.

composition is not exactly the same, no important differences have been found in the PDF patterns between the SF_E and SF_F pastes, see Figs. 4 and S26.

As previously pointed out, the raw PDF pattern for C_3S-SF_E-1.2 can be used as a reference for C-S-H gel from alite hydration. Thus, the raw PDF pattern of C_3S-SF_E-1.2 was employed to subtract the C-S-H signal of the other pastes to produce differential PDF patterns which are shown in Fig. 5. In order to do so, the reference pattern was multiplied by a factor, also stated in Fig. 5, which allows to cancel the Si—O interatomic correlation at 1.65 Å. In order words, our strategy has been to use the area of the Si—O interatomic distances to cancel out the contribution of C-S-H gel in every PDF pattern. After C-S-H signal subtraction, the differential PDF signal corresponds to the overall $Ca(OH)_2$ of the sample. These traces have two contributions, one is crystalline portlandite and the other is the excess of $Ca(OH)_2$. As it was discussed in the introduction, this excess of calcium hydroxide can be located sandwiched between tobermorite layers within the C-S-H or as independent nanocrystalline $Ca(OH)_2$ nanoparticles one to few layers thick. For reference, Fig. 5 also displays the PDF patterns of crystalline portlandite (experimentally acquired in identical conditions) and that calculated for a discrete particle of two-layer portlandite, with no periodicity. The simulated nanoparticle has 5 unit cells in the [100] and [010] directions, and 1 unit cell along the [001] direction, which means a double $Ca(OH)_2$ layer. Furthermore, the simulation was carried out by stretching the c-axis as previously reported [11].

4. Discussion

A series of hydrated tricalcium silicate with increasing contents of silica fume has been prepared with the final objective to understand the local structure of the excess of $Ca(OH)_2$ in the micrometre size C-S-H gel. It is well known that the average Ca/Si ratio of C-S-H is variable but centred close to 1.7–1.8 for neat cement pastes and that the Ca/Si ratio of crystalline (defect-free) tobermorite is just 0.83. Defect-containing tobermorite and clinotobermorite can increase this ratio twofold: i) due to the losses of silicate bridging tetrahedra, and ii) because the incorporation of charge compensating calcium-containing species like Ca^{2+}, $CaOH^+$; to values close to 1.4 [17]. Furthermore, it has been reported from atomistic simulations that the tobermorite interlayer space could host species like $CaOH^+$ and $Ca(OH)_2$ that will allow to justify Ca/Si ratios up to 2.0 in C-S-H gel [19,59]. On the other hand, systems with Ca/Si ratios above ~1.4–1.5 are often reported as a coexistence of C-S-H gel and a $Ca(OH)_2$ rich phase [11,23]. Hence, the nature of the excess of $Ca(OH)_2$ above the ~1.4 threshold remains unsettled.

The pastes have been very carefully prepared and thoroughly studied as high quality samples are needed for synchrotron pair distribution function analyses. For the $Ca(OH)_2$ excess, it is noted that just subtle differences are expected between a few-layer thick isolated $Ca(OH)_2$ nanoparticles and a few-layer thick $Ca(OH)_2$ units within the tobermorite interlayer space. Therefore, the hydration has not been arrested as this is known to slightly alter the microstructures plus inserting organic molecules within the tobermorite nanoparticles which would affect the TGA and PDF signals and corresponding analyses. The high quality of the samples has been proved by: i) full consumption of SF as measured by and ^{29}Si MAS-NMR data and RQPA; ii) full hydration of C_3S after four months; iii) a reaction degree of 90% for belite after 12 months of hydration; and iv) the absence of significant carbonation in the pastes as revealed by thermal analysis, see Fig. 2.

Crystalline portlandite consumption has been measured by thermal analysis and RQPA. In full agreement with previous reports for PC-SF blends [29] and C_3S-SF blends [60], the Ca/Si ratio of the C-S-H gel determined here for the blended pastes was 1.40–1.50 after full consumption of crystalline portlandite. These values are significantly smaller than 1.70–1.80 for neat cement pastes, which forces us to conclude that the excess of $Ca(OH)_2$ at the nanoscale can be very reactive. Moreover, complete SF reaction is observed for a blend with overall Ca/Si ratio of 1.20, meaning that all excess of $Ca(OH)_2$ is available for pozzolanic reaction. Additionally, TGA and RQPA results for the hydrated belite gave very little crystalline portlandite and consequently, the C-S-H gel has the largest Ca/Si ratio at the microscale, close to 1.90, i.e. it has the highest excess of $Ca(OH)_2$. Therefore, C_3S-SF_E-1.8 and C_2S-0SF-2.0 have quite similar overall Ca/Si ratios but different microstructures and Ca/Si local arrangement, their portlandite contents being 11.6 and 2.4 wt%, respectively.

Once, high quality samples have been prepared, the synchrotron pair distribution data were acquired and analysed. As expected, the PDF signals for the series, see Fig. 4, are mainly composed by the variable contributions of C-S-H gel and crystalline portlandite. In order to highlight this, the PDF pattern for commercial (crystalline) portlandite was also collected and added to this study. It is worth noting that crystalline portlandite is already a contentious material from the local structure point of view, as shown in Table 2. The average crystalline structure, both from neutron single crystal and synchrotron powder diffraction, should yield Ca···Ca interatomic distances along the *c*-axis of 6.11 Å. However, the stacking faults in the $Ca(OH)_2$ layers, along the *c*-axis, lead to a larger measured distance in the experimental PDF profile, 6.16 Å, see Table 2. The close analysis of Fig. 4 indicates that there are no new interatomic correlations appearing with the progress of the pozzolanic reaction. Therefore, the local structures of the original C-S-H gel, arising from the direct hydration of alite, and that of the secondary C-S-H gel, arising from the pozzolanic reaction, must be very similar. This observation allowed us to use the PDF pattern for C_3S-SF_E-1.2 as a model for C-S-H gel and to employ the well-known differential PDF methodology [23,43].

There are not many structural models for C-S-H gel with Ca/Si ratio close to 1.7–1.8. We have calculated, and included in Fig. 4, the PDF profiles from two CIF files. The first one obtained for a C-S-H gel with Ca/Si ratio of 1.75 from molecular dynamics (MD) and density functional theory (DFT) calculations [19]. The second one for a C-A-S-H gel with the following bulk stoichiometry, $(CaO)_{1.7}(Al_2O_3)_{0.05}SiO_2(H_2O)_{1.9}$, very recently obtained also from MD and DFT [20]. We acknowledge that the presence of 10 molar% aluminium can slightly affect the PDF pattern but its high Ca content make it suitable for the comparison. The calculated patterns are given at the bottom of Fig. 4 and they do not capture some features of the C-S-H experimental PDF patterns. The main mismatches are marked with stars. The reasons for such not good agreement could be: i) in the simulations the overall Ca/Si ratio of C-S-H gel is 1.70, slightly different from that of C_3S-SF_E-1.5 (the closest sample with very little crystalline portlandite); ii) C_3S-SF_E-1.5/C_3S-SF_E-1.2 samples are not fully homogeneous as shown by HR-TEM, see Table 5; and/or iii) the nature of the excess of $Ca(OH)_2$ within the interlayer space of tobermorite.

As PDF probes the local structures, it could (or help to) distinguish between the two alternatives for the excess of $Ca(OH)_2$ discussed above. In order to address this, the differential PDF profiles were obtained by subtraction as previously indicated. Fig. 5 just shows the $Ca(OH)_2$ contribution to the PDF patterns, both crystalline portlandite and excess of $Ca(OH)_2$. It is not possible to remove the contribution of crystalline portlandite by subtraction as there is not a single band which it is not overlapped and can be used as reference. The robustness of the differential PDF approach used here is exemplified by the study of C_3S-SF_E-1.8. It was shown by TA and RQPA studies that this sample contains little excess of $Ca(OH)_2$ and a large fraction of crystalline portlandite (in addition to a C-S-H gel with Ca/Si = 1.25). In agreement with this observation, its differential PDF signal is better justified with that of crystalline portlandite, see its trace in Fig. 5, with a Ca···Ca distance along the c-axis of 2.18 Å.

Now, the attention is focussed on the differential PDF patterns for C_2S-0SF-2.0 and C_3S-SF_E-1.5. C_2S-0SF-2.0 was shown to have a low amount of crystalline portlandite and a large fraction of excess of Ca $(OH)_2$. Firstly, it is acknowledged that the differences between the traces of experimental crystalline portlandite and two-layer thick

nanoportlandite are not conspicuous, see Fig. 5. Secondly, the visual inspection of data in Fig. 5 points to a slightly better agreement between the dPDF trace of C_2S-0SF-2.0 with the PDF pattern of experimental portlandite for interatomic correlations lower than 6.0 Å. Thirdly and importantly, at longer distances, the agreement nonetheless is reversed: I- The interatomic correlation close to 11.8 Å, which is very intense in crystalline portlandite and it almost vanishes for two-layer thick nanoportlandite, is very weak for the dPDFs traces of C_2S-0SF-2.0 and C_3S-SF_E-1.5, see Fig. 5. This reflects the very small particle size of the excess of $Ca(OH)_2$. However, this feature would also likely vanish for $Ca(OH)_2$ within the interlayer of tobermorite and therefore it does not help to distinguish between the two possibilities. II- The Ca···Ca interatomic correlation at 6.24 Å for C_2S-0SF-2.0 (and also for C_3S-SF_E-1.5), see also Table 2, is the longest for the studied series, see the traces in Fig. 5. These two samples are the ones with lower crystalline portlandite contents which masks this feature. This is a key observation that it is not justified, so far, with the DFT local structures for $Ca(OH)_2$-enriched C-S-H gel. Finally, it is acknowledged that our PDF data does not allow us to firmly distinguish between the two possibilities and further research is needed. Ideally, PDF data should be acquired for a C-S-H sample with overall Ca/Si ratio equal or larger than 1.70, without crystalline portlandite.

5. Conclusions

The multitechnique study, including synchrotron pair distribution function analysis, of the alite-silica fume blend series, complemented with hydrated belite, has allowed us to draw three main conclusions for the high-quality samples prepared by full consumption of silica fume without significant carbonation:

(1) In the employed experimental conditions, the secondary C-S-H gel formed by the pozzolanic reaction has the same local structure as the primary C-S-H gel formed by the alite hydration. This conclusion is drawn from the smooth variation of the PDF traces without the appearance of any additional interatomic correlation distance band.
(2) The excess $Ca(OH)_2$ formed during alite hydration is highly reactive and fully available for pozzolanic reaction as demonstrated by the Ca/Si = 1.20 sample which is well described by a defect-containing tobermorite model.
(3) Differential PDF data points toward the $Ca(OH)_2$ excess having a local structure more similar to a few-layer thick nanoportlandite stretched along the *c*-axis, than a few-unit thick $Ca(OH)_2$ slabs sandwiched between tobermorite layers. However, it is acknowledged that the current PDF data does not allow us to firmly distinguish between the two possibilities and further research is needed to fully clarify this point.

CRediT authorship contribution statement

A. Cuesta: Conceptualization, Supervision, Funding acquisition, Investigation, Formal analysis, Writing - original draft. **I. Santacruz:** Investigation, Writing - review & editing. **A.G. De la Torre:** Investigation, Writing - review & editing. **M. Dapiaggi:** Investigation, Writing - review & editing. **J.D. Zea-Garcia:** Investigation, Writing - review & editing. **M.A.G. Aranda:** Conceptualization, Investigation, Writing - original draft.

Declaration of competing interest

The authors declare that they have no known competing financial interests or personal relationships that could have appeared to influence the work reported in this paper.

Acknowledgements

This work has been supported by two research grants, BIA2017-82391-R and PID2019-104378RJ-I00, from the Spanish Science Ministry, which are co-funded by FEDER. We also thank CELLS-ALBA (Barcelona, Spain) for providing synchrotron beam time at BL04-MSPD and Alicia Manjón and Oriol Vallcorba for their assistance during the experiment. We thank the contributions from two anonymous reviewers which have improved the quality and clarity of this work.

Data availability

All in situ synchrotron X-ray powder diffraction patterns, thermal analysis and MAS-NMR spectra analysed in this article can be freely accessed on Zenodo at https://doi.org/10.5281/zenodo.4432088, and used under the Creative Commons Attribution license.

Appendix A. Supplementary data

Supplementary data to this article can be found online at https://doi.org/10.1016/j.cemconres.2021.106405.

References

[1] L. Barcelo, J. Kline, G. Walenta, E. Gartner, Cement and carbon emissions, Mater. Struct. 47 (2014) 1055–1065, https://doi.org/10.1617/s11527-013-0114-5.
[2] I. Amato, Green cement: concrete solutions, Nature. 494 (2013) 300–301, https://doi.org/10.1038/494300a.
[3] UN Environment, K.L. Scrivener, V.M. John, E. Gartner, Eco-efficient cements: potential, economically viable solutions for a low-CO2, cement-based materials industry, Cem. Concr. Res. 114 (2018) 2–26, https://doi.org/10.1016/j.cemconres.2018.03.015.
[4] C. Shi, B. Qu, J.L. Provis, Recent progress in low-carbon binders, Cem. Concr. Res. 122 (2019) 227–250, https://doi.org/10.1016/J.CEMCONRES.2019.05.009.
[5] M.C.G. Juenger, R. Snellings, S.A. Bernal, Supplementary cementitious materials: new sources, characterization, and performance insights, Cem. Concr. Res. 122 (2019) 257–273, https://doi.org/10.1016/J.CEMCONRES.2019.05.008.
[6] M.C.G. Juenger, R. Siddique, Recent advances in understanding the role of supplementary cementitious materials in concrete, Cem. Concr. Res. 78 (2015) 71–80, https://doi.org/10.1016/j.cemconres.2015.03.018.
[7] B. Lothenbach, K. Scrivener, R.D. Hooton, Supplementary cementitious materials, Cem. Concr. Res. 41 (2011) 1244–1256, https://doi.org/10.1016/j.cemconres.2010.12.001.
[8] J. Skibsted, R. Snellings, Reactivity of supplementary cementitious materials (SCMs) in cement blends, Cem. Concr. Res. 124 (2019) 105799, https://doi.org/10.1016/J.CEMCONRES.2019.105799.
[9] V.M. John, B.L. Damineli, M. Quattrone, R.G. Pileggi, Fillers in cementitious materials — experience, recent advances and future potential, Cem. Concr. Res. 114 (2018) 65–78, https://doi.org/10.1016/J.CEMCONRES.2017.09.013.
[10] H.F.W. Taylor, Cement Chemistry, 2nd ed., Thomas Telford Pub, London, UK, 1997.
[11] A. Cuesta, J.D. Zea-Garcia, D. Londono-Zuluaga, A.G. De La Torre, I. Santacruz, O. Vallcorba, M. Dapiaggi, S.G. Sanfélix, M.A.G. Aranda, Multiscale understanding of tricalcium silicate hydration reactions, Sci. Rep. 8 (2018) 8544, https://doi.org/10.1038/s41598-018-26943-y.
[12] H.M. Jennings, Refinements to colloid model of C-S-H in cement: CM-II, Cem. Concr. Res. 38 (2008) 275–289, https://doi.org/10.1016/J.CEMCONRES.2007.10.006.
[13] S. Papatzani, K. Paine, J. Calabria-Holley, A comprehensive review of the models on the nanostructure of calcium silicate hydrates, Constr. Build. Mater. 74 (2015) 219–234, https://doi.org/10.1016/j.conbuildmat.2014.10.029.
[14] E. Bonaccorsi, S. Merlino, A.R. Kampf, The crystal structure of tobermorite 14 Å (plombierite), a C-S-H phase, J. Am. Ceram. Soc. 88 (2005) 505–512, https://doi.org/10.1111/j.1551-2916.2005.00116.x.
[15] S. Merlino, E. Bonaccorsi, T. Armbruster, The real structure of tobermorite 11Å: normal and anomalous forms, OD character and polytypic modifications, Eur. J. Mineral. 13 (2001) 577–590, https://doi.org/10.1127/0935-1221/2001/0013-0577.
[16] S. Merlino, E. Bonaccorsi, T. Armbruster, Tobermorites: their real structure and order-disorder (OD) character, Am. Mineral. 84 (1999) 1613–1621. doi:doi: https://doi.org/10.2138/am-1999-1015.
[17] I.G. Richardson, Model structures for C-(A)-S-H(I), Acta Crystallogr. Sect. B Struct. Sci. Cryst. Eng. Mater. 70 (2014) 903–923, https://doi.org/10.1107/S2052520614021982.
[18] M.J. Abdolhosseini Qomi, K.J. Krakowiak, M. Bauchy, K.L. Stewart, R. Shahsavari, D. Jagannathan, D.B. Brommer, A. Baronnet, M.J. Buehler, S. Yip, F.J. Ulm, K. J. Van Vliet, R.J.M. Pellenq, Combinatorial molecular optimization of cement hydrates, Nat. Commun. 5 (2014) 1–10, https://doi.org/10.1038/ncomms5960.

[19] A. Kumar, B.J. Walder, A. Kunhi Mohamed, A. Hofstetter, B. Srinivasan, A. J. Rossini, K. Scrivener, L. Emsley, P. Bowen, The atomic-level structure of cementitious calcium silicate hydrate, J. Phys. Chem. C 121 (2017) 17188–17196, https://doi.org/10.1021/acs.jpcc.7b02439.

[20] A. Kunhi Mohamed, P. Moutzouri, P. Berruyer, B.J. Walder, J. Siramanont, J. Siramanont, M. Harris, M. Negroni, S.C. Galmarini, S.C. Parker, S.C. Parker, K. L. Scrivener, L. Emsley, P. Bowen, The atomic-level structure of cementitious calcium aluminate silicate hydrate, J. Am. Chem. Soc. 142 (2020) 11060–11071, https://doi.org/10.1021/jacs.0c02988.

[21] J.J. Thomas, J.J. Chen, H.M. Jennings, D.A. Neumann, Ca-OH bonding in the C-S-H gel phase of tricalcium silicate and white portland cement pastes measured by inelastic neutron scattering, Chem. Mater. 15 (2003) 3813–3817, https://doi.org/10.1021/cm034227f.

[22] J.J. Chen, L. Sorelli, M. Vandamme, F.-J. Ulm, G. Chanvillard, A coupled nanoindentation/SEM-EDS study on low water/cement ratio portland cement paste: evidence for C-S-H/$Ca(OH)_2$ nanocomposites, J. Am. Ceram. Soc. 93 (2010) 1484–1493, https://doi.org/10.1111/j.1551-2916.2009.03599.x.

[23] S. Grangeon, A. Fernandez-Martinez, A. Baronnet, N. Marty, A. Poulain, E. Elkaïm, C. Roosz, S. Gaboreau, P. Henocq, F. Claret, Quantitative X-ray pair distribution function analysis of nanocrystalline calcium silicate hydrates: a contribution to the understanding of cement chemistry, J. Appl. Crystallogr. 50 (2017) 14–21, https://doi.org/10.1107/S1600576716017404.

[24] O. Chaix-Pluchery, J. Bouillot, D. Ciosmak, J.C. Niepce, F. Freund, Calcium hydroxide dehydration early precursor states, J. Solid State Chem. 50 (1983) 247–255, https://doi.org/10.1016/0022-4596(83)90194-9.

[25] C. Rodriguez-Navarro, A. Burgos-Cara, F. Di Lorenzo, E. Ruiz-Agudo, K. Elert, Nonclassical crystallization of calcium hydroxide via amorphous precursors and the role of additives, Cryst. Growth Des. 20 (2020) 4418–4432, https://doi.org/10.1021/acs.cgd.0c00241.

[26] K.L. Scrivener, B. Lothenbach, N. De Belie, E. Gruyaert, J. Skibsted, R. Snellings, A. Vollpracht, TC 238-SCM: hydration and microstructure of concrete with SCMs, Mater. Struct. 48 (2015) 835–862, https://doi.org/10.1617/s11527-015-0527-4.

[27] A. Kar, I. Ray, A. Unnikrishnan, J.F. Davalos, Microanalysis and optimization-based estimation of C-S-H contents of cementitious systems containing fly ash and silica fume, Cem. Concr. Compos. 34 (2012) 419–429, https://doi.org/10.1016/j.cemconcomp.2011.09.008.

[28] J. Bizzozero, K.L. Scrivener, Limestone reaction in calcium aluminate cement - calcium sulfate systems, Cem. Concr. Res. 76 (2015) 159–169, https://doi.org/10.1016/j.cemconres.2015.05.019.

[29] J.E. Rossen, B. Lothenbach, K.L. Scrivener, Composition of C–S–H in pastes with increasing levels of silica fume addition, Cem. Concr. Res. 75 (2015) 14–22, https://doi.org/10.1016/J.CEMCONRES.2015.04.016.

[30] A.C.A. Muller, K.L. Scrivener, J. Skibsted, A.M. Gajewicz, P.J. McDonald, Influence of silica fume on the microstructure of cement pastes: new insights from 1H NMR relaxometry, Cem. Concr. Res. 74 (2015) 116–125, https://doi.org/10.1016/j.cemconres.2015.04.005.

[31] W.A. Gutteridge, J.A. Dalziel, Filler cement: the effect of the secondary component on the hydration of Portland cement. Part I. A fine non-hydraulic filler, Cem. Concr. Res. 20 (1990) 778–782. doi:https://doi.org/10.1016/0008-8846(90)90011-L.

[32] T. Oey, A. Kumar, J.W. Bullard, N. Neithalath, G. Sant, The filler effect: the influence of filler content and surface area on cementitious reaction rates, J. Am. Ceram. Soc. 96 (2013) 1978–1990, https://doi.org/10.1111/jace.12264.

[33] J. Lapeyre, A. Kumar, Influence of pozzolanic additives on hydration mechanisms of tricalcium silicate, J. Am. Ceram. Soc. 101 (2018) 3557–3574, https://doi.org/10.1111/jace.15518.

[34] M. Bhattacharya, K.V. Harish, An integrated approach for studying the hydration of portland cement systems containing silica fume, Constr. Build. Mater. 188 (2018) 1179–1192, https://doi.org/10.1016/j.conbuildmat.2018.08.114.

[35] W. Xu, T.Y. Lo, W. Wang, D. Ouyang, P. Wang, F. Xing, Pozzolanic reactivity of silica fume and ground rice husk ash as reactive silica in a cementitious system: a comparative study, Materials (Basel). 9 (2016). doi:https://doi.org/10.3390/ma9030146.

[36] T. Egami, S.J.L. Billinge, Underneath the Bragg Peaks: Structural Analysis of Complex Materials., 2nd ed., Elsevier Science, Pergamon, 2012. https://www.elsevier.com/books/underneath-the-bragg-peaks/egami/978-0-08-097133-9.

[37] S.J.L. Billinge, M.G. Kanatzidis, Beyond crystallography: the study of disorder, nanocrystallinity and crystallographically challenged materials with pair distribution functions, Chem. Commun. 0 (2004) 749–760. doi:https://doi.org/10.1039/b309577k.

[38] A. Cuesta, R. Ichikawa, D. Londono-Zuluaga, A.G. De la Torre, I. Santacruz, X. Turrillas, M.A.G. Aranda, Aluminum hydroxide gel characterization within a calcium aluminate cement paste by combined Pair Distribution Function and Rietveld analyses, Cem. Concr. Res. 96 (2017) 1–12, https://doi.org/10.1016/j.cemconres.2017.02.025.

[39] L.B. Skinner, S.R. Chae, C.J. Benmore, H.R. Wenk, P.J.M. Monteiro, Nanostructure of calcium silicate hydrates in cements, Phys. Rev. Lett. 104 (2010) 195502, https://doi.org/10.1103/PhysRevLett.104.195502.

[40] A.E. Morandeau, C.E. White, In situ X-ray pair distribution function analysis of accelerated carbonation of a synthetic calcium–silicate–hydrate gel, J. Mater. Chem. A 3 (2015) 8597–8605, https://doi.org/10.1039/C5TA00348B.

[41] S. Bae, H. Jee, M. Kanematsu, A. Shiro, A. Machida, T. Watanuki, T. Shobu, H. Suzuki, Pair distribution function analysis of nanostructural deformation of calcium silicate hydrate under compressive stress, J. Am. Ceram. Soc. 101 (2018) 408–418, https://doi.org/10.1111/jace.15185.

[42] C.E. White, Effects of temperature on the atomic structure of synthetic calcium–silicate–deuterate gels: a neutron pair distribution function investigation, Cem. Concr. Res. 79 (2016) 93–100, https://doi.org/10.1016/J.CEMCONRES.2015.09.001.

[43] C.E. White, L.L. Daemen, M. Hartl, K. Page, Intrinsic differences in atomic ordering of calcium (alumino)silicate hydrates in conventional and alkali-activated cements, Cem. Concr. Res. 67 (2015) 66–73, https://doi.org/10.1016/j.cemconres.2014.08.006.

[44] A. Cuesta, M.A.G. Aranda, J. Sanz, A.G. De La Torre, E.R. Losilla, Mechanism of stabilization of dicalcium silicate solid solution with aluminium, Dalt. Trans. 43 (2014) 2176–2182, https://doi.org/10.1039/c3dt52194j.

[45] F. Fauth, I. Peral, C. Popescu, M. Knapp, The new material science powder diffraction beamline at ALBA synchrotron, Powder Diffract. 28 (2013) S360–S370, https://doi.org/10.1017/S0885715613000900.

[46] A.C. Larson, R.B. Von Dreele, General structure analysis system (GSAS), Los Alamos Natl. Lab. Rep. LAUR. 748 (2004) 86–748.

[47] P. Thompson, D.E. Cox, J.B. Hastings, Rietveld refinement of Debye-Scherrer synchrotron X-ray data from A1203, J. Appl. Crystallogr. 20 (1987) 79–83, https://doi.org/10.1107/S0021889887087090.

[48] A.G. De La Torre, S. Bruque, M.A.G. Aranda, Rietveld quantitative amorphous content analysis, J. Appl. Crystallogr. 34 (2001) 196–202, https://doi.org/10.1107/S0021889801002485.

[49] P. Juhas, T. Davis, C.L. Farrow, S.J.L. Billinge, PDFgetX3: a rapid and highly automatable program for processing powder diffraction data into total scattering pair distribution functions, J. Appl. Crystallogr. 46 (2013) 560–566, https://doi.org/10.1107/S0021889813005190.

[50] O. Vallcorba, D1Dplot: powder diffraction data processing - ALBA Synchrotron. https://www.cells.es/en/beamlines/bl04-mspd/preparing-your-experiment, 2019.

[51] P. Juhás, C.L. Farrow, X. Yang, K.R. Knox, S.J.L. Billinge, Complex modeling: a strategy and software program for combining multiple information sources to solve ill posed structure and nanostructure inverse problems, Acta Crystallogr. Sect. A Found. Adv. 71 (2015) 562–568, https://doi.org/10.1107/S2053273315014473.

[52] M. Palacios, H. Kazemi-Kamyad, S. Mantellato, P. Bowen, Laser diffraction and gas adsorption techniques, in: K. Scrivener, R. Snellings (Eds.), A Pract. Guid. to Microstruct. Anal. Cem. Mater, CRC Press, Boca Raton, 2016, pp. 445–484.

[53] O. Chaix-Pluchery, J. Pannetier, J. Bouillot, J.C. Niepce, Structural prereactional transformations in Ca(OH)2, J. Solid State Chem. 67 (1987) 225–234, https://doi.org/10.1016/0022-4596(87)90358-6.

[54] S. Goñi, F. Puertas, M.S. Hernández, M. Palacios, A. Guerrero, J.S. Dolado, B. Zanga, F. Baroni, Quantitative study of hydration of C3S and C2S by thermal analysis: evolution and composition of C-S-H gels formed, J. Therm. Anal. Calorim. 102 (2010) 965–973, https://doi.org/10.1007/s10973-010-0816-7.

[55] A. Mendes, W.P. Gates, J.G. Sanjayan, F. Collins, NMR, XRD, IR and synchrotron NEXAFS spectroscopic studies of OPC and OPC/slag cement paste hydrates, Mater. Struct. 44 (2011) 1773–1791, https://doi.org/10.1617/s11527-011-9737-6.

[56] I. Richardson, The nature of C-S-H in hardened cements, Cem. Concr. Res. 29 (1999) 1131–1147, https://doi.org/10.1016/S0008-8846(99)00168-4.

[57] M.J. Sánchez-Herrero, A. Fernández-Jiménez, Á. Palomo, Alkaline hydration of C2S and C3S, J. Am. Ceram. Soc. 99 (2016) 604–611, https://doi.org/10.1111/jace.13985.

[58] B. Lothenbach, P. Durdzinski, K. De Weerdt, Thermogravimetric analysis, in: B.L. K. Scrivener, R. Snellings (Eds.), A Pract. Guid. to Microstruct. Anal. Cem. Mater, CRC Press, Boca Raton, 2016, pp. 177–211.

[59] A. Kunhi Mohamed, S.C. Parker, P. Bowen, S. Galmarini, An atomistic building block description of C-S-H - towards a realistic C-S-H model, Cem. Concr. Res. 107 (2018) 221–235, https://doi.org/10.1016/j.cemconres.2018.01.007.

[60] Z.-Q. Wu, J.F. Young, The hydration of tricalcium silicate in the presence of colloidal silica, J. Mater. Sci. 19 (1984) 3477–3486, https://doi.org/10.1007/bf00552262.